

TWO-COMPONENT HORIZONTAL MOTION VECTORS FROM THE RAMAN-SHIFTED EYE-SAFE AEROSOL LIDAR (REAL)

Shane D. Mayor

Department of Physics, California State University Chico, sdmayor@csuchico.edu

ABSTRACT

Two-component horizontal motion vectors of aerosol features were calculated by applying a cross-correlation algorithm to square image blocks extracted from consecutive pairs of elastic backscatter lidar scans. The resulting vector components were compared with corresponding horizontal wind components from tower-mounted sonic anemometers located at the center of the image blocks. 180 245 pairs of vectors derived from 75 days of field data collected between 19 March and 11 June 2007 were used in the analysis. Examples of time-series comparisons from various boundary layer states and statistical results of the comparisons will be presented. The correlation between the lidar-derived motion components and sonic anemometer wind components tends to be highest during light wind conditions with low TKE. Examples of two-dimensional and two-component vector flow fields will also be presented.

1. INTRODUCTION

This paper is a condensed version of a manuscript recently accepted for publication in the *Journal of Atmospheric and Oceanic Technology* [1]. It describes 2-component horizontal wind measurements made by applying a cross-correlation motion estimation algorithm to scans from the Raman-shifted Eye-safe Aerosol Lidar (REAL) [2] (see Fig. 1) during the 2007 Canopy Horizontal Array Turbulence Study (CHATS) [3]. Previous work on the topic of deriving winds from elastic backscatter lidar data are described in [4-12]. The present work is unique because it employs an *eye-safe* lidar system and the derived vector components are compared with in situ velocity measurements within the scan area. The REAL transmits 6 ns pulses at a pulse rate of 10 Hz and operates at 1.54 microns wavelength.



Figure 1: The Raman-shifted Eye-safe Aerosol Lidar (REAL) at the California State University Chico Farm.

2. EXPERIMENTAL SETUP

CHATS took place in Dixon, California, from mid-March through early-June of 2007. The focus of the experiment was a horizontal array of sonic anemometers located approximately 100 m south of a 30 m tall vertical instrumented tower in a large walnut orchard. The REAL was located 1.61 km directly north of the 30 m tower. PPI scans were directed toward the south as shown in Fig. 2. The lidar scan plane intersected the tower between 18 and 20 m AGL (see Fig. 3). Because of uncertainty in the exact altitude of the lidar beam at the tower and frequent strong vertical wind shear just above the trees, no attempt has been made to compare mean lidar-derived velocities with mean sonic anemometer data. Therefore, in this paper (and in [1]), only the vector components resulting from pairs of lidar scans are compared with anemometer data averaged over the time it took the lidar to collect a pair of scans. A visual depiction of how the lidar-derived vectors were calculated and compared with the sonic anemometer time series data is shown in Fig. 4.



Figure 2. Plan-view of the experimental area. The shaded regions from $150^{\circ} - 210^{\circ}$ and $175^{\circ} - 185^{\circ}$ azimuth represent the areas covered by “wide” and “narrow” PPI scans, respectively. The vertical tower (VT) was located 1.61 km directly south of the REAL. The white squares centered on the VT represent the image blocks extracted from the gridded PPI scan data that were used to compute motion vectors via the cross-correlation technique.

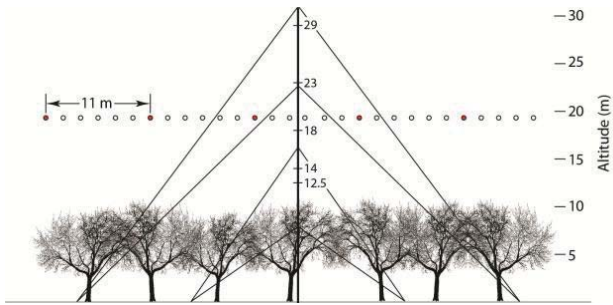


Figure 3. Diagram showing the approximate altitude, spacing, and size of REAL laser pulses with respect to the tree tops and the vertical tower at CHATS. This diagram is an east-west cross section looking either towards (north) or away (south) from the lidar. Shaded circles represent laser pulses from one scan at an azimuthal scan rate of 4° s^{-1} . At this scan rate, the pulses are spaced 11 m apart at 1.61 km range from the lidar.

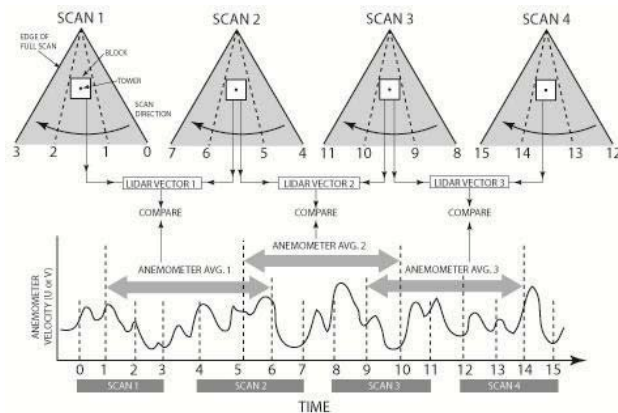


Figure 4. Visual depiction of how anemometer time series data were averaged for comparison with the vectors derived from lidar scans. This example considers a series of four consecutive PPI scans that result in three vectors. The anemometer data are averaged over the periods corresponding to when the lidar's beam enters the block on the first scan (positions 1, 5, and 9 in time) and exits the block on the subsequent scan (positions 6, 10 and 14 in time).

3. TIME-SERIES COMPARISONS

The experiment resulted in over 1000 hours of time series comparisons like those shown in Fig. 5, 6, and 7. In the time-series comparisons, the colored lines are of the slightly averaged sonic anemometer wind components (u is the east-west component; v is the north-south component) and the black points are the result of the cross-correlation algorithm when applied to a square block centered on the tower location. Four block sizes were used (shown as squares on centered on tower in Fig. 2). Larger blocks result in less scatter in the lidar-derived points and better correlations with the sonic anemometer data. In some cases it is possible to

achieve good results with the smallest block size ($250 \text{ m} \times 250 \text{ m}$) as shown in Fig. 5. However, during more windy and turbulent conditions, it is necessary to use much larger block sizes. The lidar-derived vector components shown in Figs. 6 and 7 used 1 km^2 blocks.

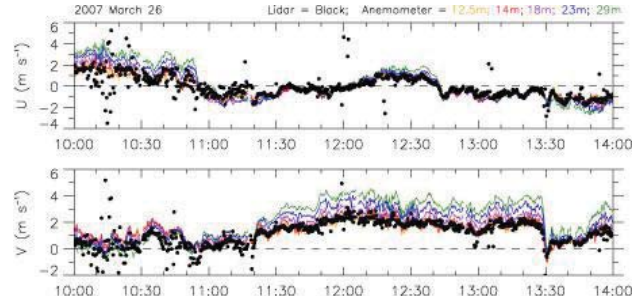


Figure 5. Time series of lidar-derived (black points) and averaged sonic anemometer (color traces) velocity components for a 4-hour period during light wind conditions. A $250 \text{ m} \times 250 \text{ m}$ block size was used for the lidar-derived velocity estimates.

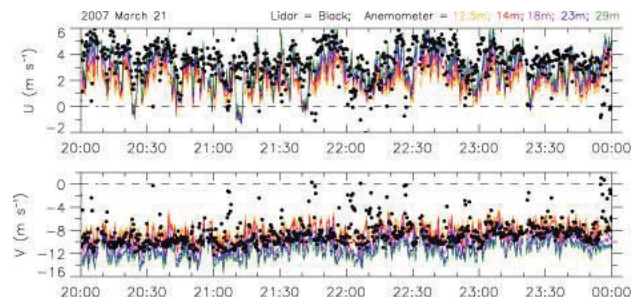


Figure 6. Time series of lidar-derived (black points) and averaged sonic anemometer (color traces) velocity components for a 4-hour period during strong wind conditions. A 1 km^2 block size was used for the lidar-derived velocity estimates.

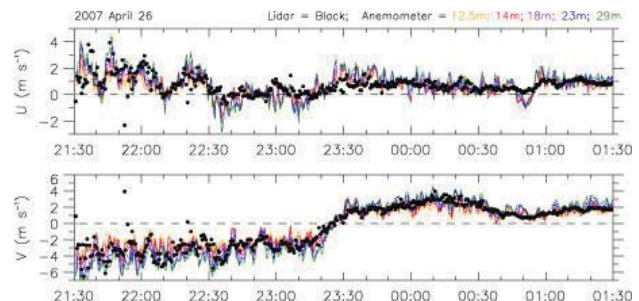


Figure 7. Time series of lidar-derived (black points) and averaged sonic anemometer (color traces) velocity components for a 4-hour period during moderate wind conditions with a frontal passage. A 1 km^2 block size was used for the lidar-derived velocity estimates.

Figure 5 is a good example of the typical performance at night when winds are light and variable and the atmosphere tends toward stability. In general, it was found that the cross-correlation provides the best correlation with the sonic anemometer data at night.

Figure 6 is an example of what can be achieved during a very windy day when the boundary layer is turbulent and near-neutral. During these conditions, the point to point correlation is not that good, but the cross-correlation algorithm is capable of capturing the mean flow. Again, as pointed out in the previous section, means were not computed and compared due to uncertainty of the precise altitude of the laser beam at the tower and the existence of strong vertical wind shear immediately above the trees.

Figure 7 shows a near reversal in flow direction with the passage of a density current front. The details of this case, and 6 others like it, are described in detail in [13]. This case represents a more moderate range of wind speeds than those shown in Figs. 5 and 6.

In all, 180 245 pairs of vectors were compared for a wide variety of weather conditions over the nearly three month field experiment. For each vector computed from the lidar data, several scalar variables were recorded. These include wind speed (from the sonic anemometer data); turbulent kinetic energy (TKE, measured from sonic anemometers); maximum of the cross-correlation function (CCF max, from the lidar data); and mean signal to noise ratio (SNR) of the lidar data in the block area. It was found that the correlation between lidar-derived velocity components and sonic anemometer velocity components became worse as the TKE or wind speed increased and became better as the mean SNR or CCF max increased.

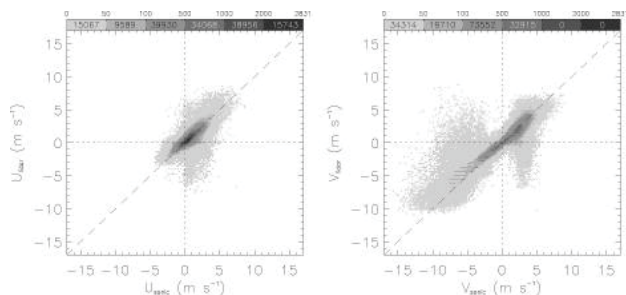


Figure 8. Distribution of 18 m AGL sonic anemometer wind components versus aerosol motion components derived from the lidar data after application of the QC model. The linear correlation coefficient for the u-component comparisons (left panel) is 0.75 and the v-component comparisons (right panel) is 0.90.

A quality control (QC) model was developed and is described in detail in [1]. It uses the sonic anemometer data as a reference to generate equations that can be used to predict the difference based on the mean SNR and CCF max. This is useful for discarding low quality wind estimates—especially when the algorithm is applied to areas on the scan without co-located sonic anemometer data.

Figure 8 is a shaded scatterplot of the comparisons after application of the quality control model. Because of the high density of data points, the number of occurrences of comparisons was accumulated into 0.2 m s^{-1} by 0.2 m s^{-1} bins and shaded according the gray shade scale at the top. We chose to shade bins (even those containing only 1 data point) to reveal the behavior of the algorithm over all conditions including infrequent high wind events. The vast majority of data points lie within the darker shaded region along the dashed identity line. It is important to note that the distribution is also the result of the non-uniform distribution of wind speeds and directions that were experienced during CHATS.

4. TWO-DIMENSIONAL WIND FIELDS

The cross-correlation algorithm can be applied to a grid of locations over the entire scan area. Doing so results in vector flow fields such as those shown in Figs. 9 and 10. The flow field shown in Fig. 9 is the lidar estimate of the two-component horizontal wind field at 00:19:47 UTC on 26 March 2007. It was calculated using 1 km^2 blocks and one pair of scans separated by 17 s. Vectors were calculated every 10 m in the horizontal Cartesian dimensions and streamlines were launched every 100 m. At the time, a vortex was located 2.7 km south and 0.2 km west of the lidar. The flow field also reveals a saddle point 3.5 km south of the lidar and 0.3 km east of the lidar. In situ data show light ($< 3 \text{ m s}^{-1}$) and variable winds until approximately 01:30 UTC when a uniform WSW flow swept across the region.

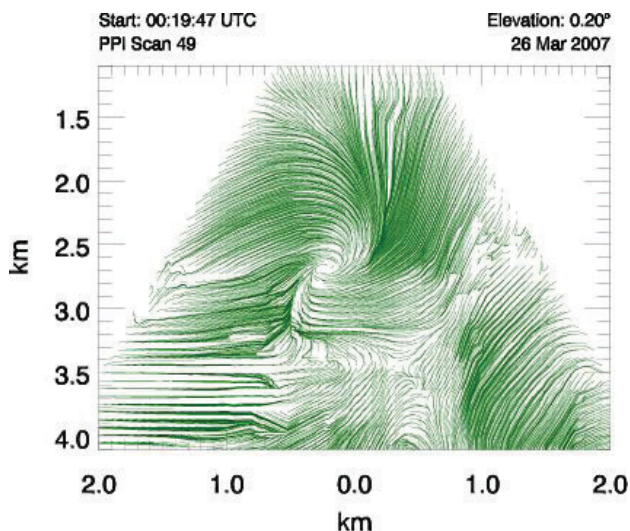


Figure 9. Streamlines from the application of the cross-correlation algorithm to a pair of PPI scans through a convective afternoon atmospheric surface layer when winds were light and variable. Scans were separated in time by 17 s. A block size of 1 km^2 was applied at the grid interval of 10 m. Streamlines were launched every 100 m.

Figure 10 reveals the flow field when a density current front [13] approximately bisected the scans area. Flow north of the front was northerly (indicated by blue streamlines) and flow south of the front was southerly (indicated by red streamlines). However, in addition to the narrow band of convergence at the front, the lidar-derived flow fields reveal eastward transport of air that flows into a vortex centered 3.7 km south and 1.5 km east of the lidar. These observations show that flow may not rise over the front uniformly and rather may be transported significant horizontal distances before being swept up into narrow and rapidly rising currents.

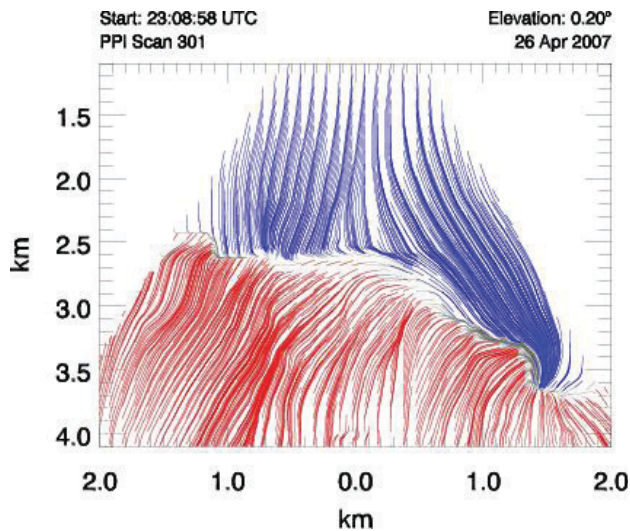


Figure 10. Streamlines from the application of the cross-correlation algorithm to a pair of PPI scans when a density current front was advancing from the south. Streamlines are colored according to the sign of the v component with blue indicating northerly flow north of the front and red indicating southerly flow south of the front. The scans were separated by 30 s and a 1 km^2 block was applied at the grid spacing of 10 m. Streamlines were launched every 100 m.

5. NEXT STEPS

The CSU Chico Atmospheric Lidar Group is currently working on several fronts to improve this capability. One effort involves stabilization and remote control of the lidar system for long-term and unattended operation. Another effort involves real-time calculation of the wind fields using graphical processing units. We are also developing of software to visualize the flow-fields in near-real-time from any web-browser.

ACKNOWLEDGMENTS

This work was supported by NSF AGS 0924407.

REFERENCES

1. Mayor, S. D., J. P. Lowe, and C. F. Mauzey, 2012: Two-component horizontal aerosol motion vectors in

the atmospheric surface layer from a cross-correlation algorithm applied to elastic backscatter lidar data, *J. Atmos. Ocean. Technol.* In press.

2. Mayor, S. D., S. M. Spuler, B. M. Morley, and E. Loew, 2012: Polarization lidar at 1.54-microns and observations of plumes from aerosol generators, *Opt. Eng.*, **46**, DOI: 10.1117/12.781902.

3. Patton E. G., et al., 2011: The Canopy Horizontal Array Turbulence Study (CHATS), *Bull. Amer. Meteor. Soc.*, **92**, pp. 593-611.

4. Eloranta, E. W., J. M. King, and J. A. Weinman, 1975: The determination of wind speeds in the boundary layer by monostatic lidar. *J. Appl. Meteor.*, **14**, pp. 1485-1489.

5. Sroga, J. T., E. W. Eloranta, and T. Barber, 1980: Lidar measurements of wind velocity profiles in the boundary layer. *J. Appl. Meteor.*, **19**, 598-605.

6. Kunkel, K. E., E. W. Eloranta, and J. Weinman, 1980: Remote determination of winds, turbulence spectra and energy dissipation rates in the boundary layer from lidar measurements. *J. Atmos. Sci.*, **37**, 978-985.

7. Sasano, Y., H. Hirohara, T. Yamasaki, H. Shimizu, N. Takeuchi, and T. Kawamura, 1982: Horizontal wind vector determination from the displacement of aerosol distribution patterns observed by a scanning lidar. *J. Appl. Meteor.*, **21**, 1516-1523.

8. Hooper, W. P. and E. W. Eloranta, 1986: Lidar measurements of wind in the planetary boundary layer: the method, accuracy and results from joint measurements with radiosonde and kytoon. *J. Clim. Appl. Meteor.*, **25**, 990-1001.

9. Kolev, I., O. Parvanov, and B. Kaprielov, 1988: Lidar determination of winds by aerosol inhomogeneities: motion velocity in the planetary boundary layer. *Appl. Optics*, **27**, 2524-2531.

10. Schols, J. L. and E. W. Eloranta, 1992: The calculation of area-averaged vertical profiles of the horizontal wind velocity from volume imaging lidar data. *J. Geophys. Res.*, **97**, 18 395-18 407.

11. Piironen, A. K. and E. W. Eloranta, 1995: Accuracy analysis of wind profiles calculated from volume imaging lidar data. *J. Geophys. Res.*, **100**, 25 559-25 567.

12. Mayor, S. D. and E. W. Eloranta, 2001: Two-dimensional vector wind fields from volume imaging lidar data. *J. Appl. Meteor.*, **40**, 1331-1346.

13. Mayor, S. D., 2011: Observations of seven density current fronts in Dixon, California. *Mon. Wea. Rev.* **139**, 1338-1351.